SCIENTIFIC REPORTS

OPEN

# New insights into the origin of remote PPG signals in visible light and infrared

Received: 15 January 2018
Accepted: 3 May 2018
Published online: 31 May 2018

Andreia V. Moço[1], Sander Stuijk[1] & Gerard de Haan[1,2]

**Remote photoplethysmography (PPG) is an optical measurement technique with established applications in vital signs monitoring. Recently, the consensual understanding of blood volume variations (BVVs) as the origin of PPG signals was challenged, raising validity concerns about the remote $SpO_2$ methodology. Recognizing the imperative for new opto-physiological evidence, this investigation supports the volumetric hypothesis with living skin experiments and Monte Carlo simulations of remote PPG-amplitude in visible light (VIS) and infrared (IR). Multilayered models of the skin were developed to simulate the separate contributions from skin layers containing pulsatile arterioles to the PPG signal in the 450–1000 nm range. The simulated spectra were qualitatively compared with observations of the resting and compressed finger pad, and complemented with videocapillaroscopy. Our results indicate that remote PPG systems indeed probe arterial blood. Green wavelengths probe dermal arterioles while red-IR wavelengths also reach subcutaneous BVVs. Owing to stable penetration depths, the red-IR diagnostic window promotes the invariance of $SpO_2$ measurements to skin non-homogeneities.**

Photoplethysmography (PPG) is an optical measurement technique that has advanced technically, achieving ubiquity in current clinical settings[1] and the status of enabling technology for non-obtrusive innovations in pulse-rate and $SpO_2$ monitoring[2–5]. Various sensing modalities are available for probing PPG signals. Its fundamental distinction is in whether signals are acquired in transmission or in re ection mode. Transmission-based acquisition requires the illuminating source and photosensor to face opposing sides of the tissue, whereas the latter has these elements on the same side. Transmission-mode PPG results from minute cardiac-related modulations of skin absorbance and is ubiquitous in most nger pulse oximeters (see Fig. 1a).

Camera-based systems can operate in transmission-mode[6], but are better suited for remote re ectance measurements. Remote PPG allows that the pulse-rate is extracted, preferentially, at green wavelengths, though a quest for motion robustness deems necessary that multiple wavelength bands (color-channels) are combined[7]. e red-IR diagnostic window has also been shown suitable for PPG-based measurements, including $SpO_2$[8].

PPG systems continue to mature by exploring of the PPG signal's frequency diversity. Multispectral PPG data, in VIS–IR, may nd clinical value in skin health assessments[9,10]. While multispectral cameras remain prohibitively expensive and computationally heavy, multispectral PPG can be acquired by coupling a spectrometer with an optical ber probe (OFP; see Fig. 1c). Since there is contact of the probe with the skin, we refer to this setting as re ection-mode acquisition.

## Importance of investigating the origin of the PPG signal

It may come as a surprise that the PPG-based techniques and applications have developed more than the opto-physiological knowledge pertaining to the origin of the signal, which remains vaguely referred to as arterial blood volume variations (BVVs) occurring at every cardiac heart beating within the microvascular bed of tissue. Still, the understanding of PPG as BVVs, which we shall refer to as the volumetric model, has been able to support the working principle of current PPG-based applications. In particular, the volumetric model provides a rationale for using PPG as a surrogate of the arterial blood oxygenation curve. e enabling principle is the dependency between normalized PPG-amplitude ratios at red–IR wavelengths, and the relative proportion between oxygenated and non-oxygenated haemoglobin absorption[3,11].

[1]Department of Electrical Engineering, Eindhoven University of Technology, 5612AZ, Eindhoven, The Netherlands. [2]Philips Innovation Group, Philips Research, High Tech Campus 36, 5656AE, Eindhoven, The Netherlands. Correspondence and requests for materials should be addressed to A.V.M. (email: a.moco@tue.nl)

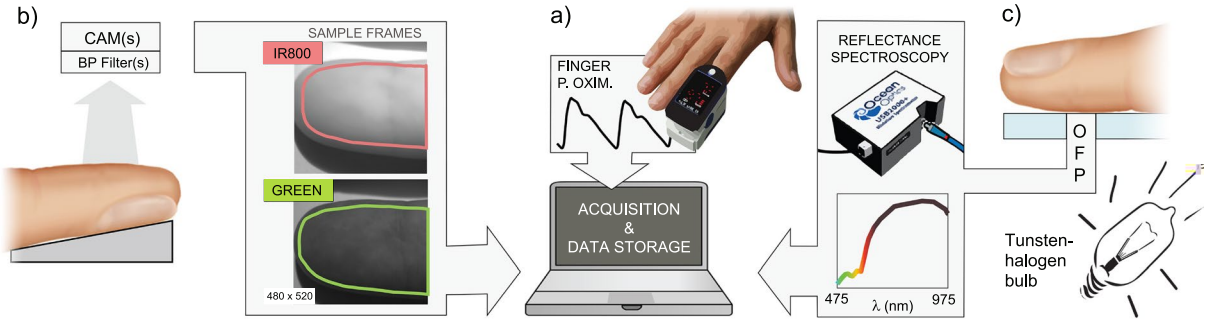


**Figure 1.** PPG signals can be acquired (**a**) in transmission-mode, e.g., by nger pulse oximetry, (**b**) remotely, or (**c**) in re ectance-mode, e.g., by using a spectrometer (OFP, optical ber probe). e gure was created by A. Moço.

e volumetric model is consensual but not unique[1]. For example, ow variations have been suggested as a mechanism for inducing light re ectance variations[12,13]. Naslund *et al.*[12] observed re ection-mode PPG signals by using IR wavelengths in the patellar bone, a site where vessel wall distentions are not theoretically possible. It remains uncertain whether this observation is spurious contamination by surrounding pulsatile tissue. More reliable optical insights on PPG generation may be obtained by investigating blood ow in phantoms. Lindberg[13] showed that blood re ection changes if a liquid solution containing red blood cells (RBCs) ows in a rigid tube. When the ow velocity and concentration of the solution are such that periodic RBC aggregation takes place (i.e., haematocrit levels above 38%), the blood re ection re ects the changes in the orientation and deformability of the RBCs[13]. On a similar setup, Shvartsman[14] simulated pulsatile blood ow and con rmed that PPG-like signals are associated with geometric changes in RBC aggregation[14].

Recently, Kamshilin *et al.*[15] reported con icting observations with the volumetric model[16]. One of such observations were counter-phase PPG signals in the vicinity of the radial or brachial artery, which are simply motion artifacts[17,18]. A more interesting argument raised against the volumetric model was the apparent paradox that the PPG-amplitude peaks in green, although it would not, theoretically, even reach pulsating arterioles. Gently compressing the skin against a glass plate increases the green PPG-amplitude further, which, again, appears to nd no explanation in the volumetric model.

Consequently, a new theory was proposed, drawing attention to elastic deformations of the dermis as dominant mechanism of PPG formation. e increasing transmural pressure of the arteries during systole would compress the dermal connective tissue and increase the overall the capillary density. ese deformations would explain the observed gains under compression. However, if arterial BVVs are not the origin of PPG, concerns emerge when it comes to the validity of PPG-based $SpO_2$ measurements. In fact, if the total dermal tissue is periodically compressed, then PPG-based $SpO_2$ readings would not be possible as these would be severely contaminated by venous pulsations.

Supporting and broadening the application scopes of PPG requires that the depth-origin of the signal is con rmed and its origin explained. us, it is imperative that the volumetric model is revised in light of the recent experiments devised by Kamshilin[15]. If it could be shown that even visible light penetrates deep enough to interact with arterioles, then the con dence on the volumetric model would be enforced. In this paper we tackle this topic under the hypothesis that the volumetric model is true and take a combined numerical and experimental approach. e skin was modeled as multilayered media with optical properties that translate its anatomophysiology[19]. en the Monte Carlo method was applied to simulate the PPG-amplitude spectra; its veri cation on living skin validated, indirectly, the volumetric model assumption.

## Modeling the skin's microvasculature

e inhomogeneity of the microvasculature was accounted by representing the non-glabrous skin structure as a medium split into six stacked horizontal layers (see Fig. 2a). e rst layer corresponds to the epidermis (EPI), which is bloodless[20] and consists of mostly dead or dehydrated cells and no melanosoms. e thickness of the epidermis is highly skin-site dependent, but 0.8 mm is reasonable for the nger pad. e dermis was subdivided into four layers with di erent blood concentrations, which are as follows[21]: capillary loops (CL; 150–200 $\mu$m thick); upper plexus (UP; 80 $\mu$m thick), reticular dermis (RD; 1400–3000 $\mu$m thick); and deep plexus (DP; 80–700 $\mu$m thick). e arterial compartment in the plexuses and RD represent arterioles supplying the entire tissue volume and venules collecting the returning venous blood. e deepest layer of the model is the subcutis (SC; or hypodermis), which accounts for fat, connective tissue and pulsating arterioles or arteries.

Our hypothesis that BVVs are located at the dermal plexuses, RD and SC is partly in agreement with prior work of Reuss[22], where it is assumed that only the plexuses contribute to PPG formation, but not with Huelsbusch[23], who modeled the PPG's origin at the capillary loops only. However, Huelsbusch's PPG-amplitude spectrum largely underestimated the relative amplitude of signals in red-IR wavelengths, suggesting the incorrectness of this parameter setting.

We implemented models that mimic the opto-physiological contribution of the skin layers to the total reflectance-mode PPG spectra, separately, for normal and compressed skin (see Fig. 2a,b, respectively). Recognizing each of these contributions as the layer's "signatures", the overall remote PPG signal is in fact a

mixture of the dermal and subdermal signatures. A useful as proof-of-concept for the volumetric model hypothesis is to isolate and demonstrate these signatures. However, the mixing weights are unknown, which is also why the compression intervention is valuable in this study.

Strong compression, yet below the systolic pressure level, is a simple intervention to block the dermal BVVs and blanch the skin, hence isolating the signatures from deeper pulsating structures in the PPG spectra of the compressed skin and allowing the incident light to reach deeper layers. Under full occlusion of the upper dermis, only the DP and SC remain pulsatile, and the removal of venous blood leads to its contributions being much stronger than in normal conditions. When sustained, metabolites accumulate and arterial vasodilation is also triggered[24,25]

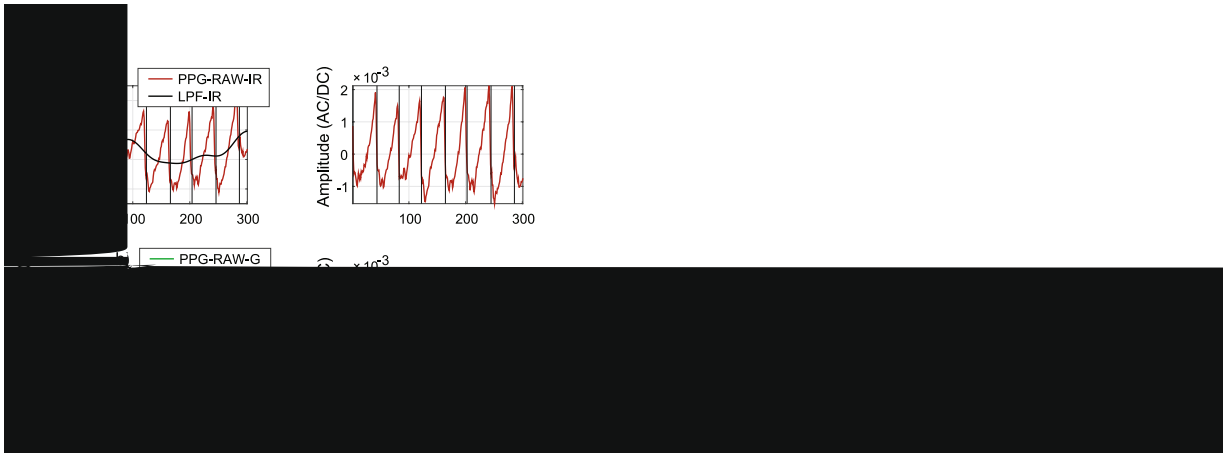


bandwidth, 559/34 nm) and in IR (800/12 nm). Speci cally, Fig. 3a,b show the average skin pixel intensity in consecutive samples for the green and IR recordings; i.e., "raw" PPG signals are the absolute di use re ectance of the skin over time. Similarly, Fig. 3c,d illustrate the normalized signals, resulting in periodic and zero-mean temporal series whose amplitude is typically upper bounded by 0.1. Consistent with the literature[2], we denote this format as "AC/DC" (abbreviation,"alternate current" over "direct current"). AC/DC normalization is performed by dividing the "raw PPG" (units, least signi cant bits; l.s.b.) by its low-pass ltered component (LPF).

A er pixel averaging and normalization, two periodic and light-invariant PPG streams are obtained. ese are polluted by sensor noise but ensemble-averaging (EA) cardiac cycles eliminates noise while retaining signal information (see Fig. 3e). Note that the amplitude di erence between green and IR signals is consistent with the wavelength dependence of PPG and with the expectation that green and IR interact with the vasculature at di erent depths[9].

Waveform dissimilarity is further evidenced when the EA waveforms are truncated to the fundamental of the pulse-rate frequency and scaled to unity (see Fig. 3f,g). An obvious feature for quantifying dissimilarity between two waveforms is the relative amplitude w.r.t. a reference wavelength. For example, when the reference is set at 800 nm, a ratio-of-ratios, $R$, can be computed as the standard deviation of the normalized green over IR (center wavelength, 800 nm) waveforms. For the pair of recordings depicted in Fig. 3, we measured an R of 2.9, but inter-individual di erences can be large. On a small sample size ($N = 4$), R was estimated to be $1.8 \pm 0.8$. Subsequently, this range will be considered for calibrating the remote PPG spectra. Another useful feature for quantifying dissimilarity is the phase shi , $P$, which we illustrate at the fundamental of the signals. A non-zero $P$ between wavelengths supports that the microvasculature is probed at di erent depths. In Fig. 3g, P was measured as 20 degrees, but test-retest experiments in other subjects suggest that the range of $P$ is broad, ranging up to 30 degrees.

*Videocapillaroscopy.* Observing the capillary loops at the nger nail fold during PPG signal acquisition is insightful to investigate a possible contribution of capillaries to PPG. Owing to the low epidermal thickness at the nail fold, the capillary loops and arterioles are found as close to the surface as 0.28–0.43 mm and $>0.43$ mm, respectively[26], and can be reached using green light. Figure 4a shows our videocapillaroscopic setup and Fig. 4b a stable PPG segment, overlapped and its peaks and valleys in one subject.

When the frames corresponding to these critical instants are registered and averaged, separately for systole and diastole, the corresponding super-resolved images of the capillary loops are obtained (see Fig. 4(c,d)). e peak-to-peak (p2p) amplitude of the signal remains fairly stable during the selected segment and no di erences were apparent in the density of visible capillaries. An useful approach to continue exploring data is to perform the normalized di erence between the systolic and diastolic frames. e outcome is a PPG-amplitude image (PPGI, amplitude expressed as AC/DC-p2p; see Fig. 4e) which indicates that the PPG-amplitude is strongest where the blood concentration is highest (identi ed as darker regions in Fig. 4d). is interpretation is not confounded by the local density of capillary loops, which is fairly even across the imaged area. PPGI further shows that the gradient of the PPG strength varies smoothly across the skin surface and does not re ect the activity of isolated or clustered loops. is supports the hypothesis that the PPG in green is modulated by upper dermal arterioles.

*Spectroscopic measurements of PPG on normal and compressed skin.* is section shows our di use re ectance (DR) and re ectance-PPG spectra. 16 subjects were measured at normal conditions and under compression. One subject was excluded because the PPG signal in normal conditions was hidden by sensor noise. Figure 5a contrasts average DR spectra from the remaining 15 subjects of our dataset. e di erence between these plots, $\Delta$DR, is a wavelength-dependent function with relative peaks close to haemoglobin absorption (542 nm, 582 nm; see Fig. 5b).

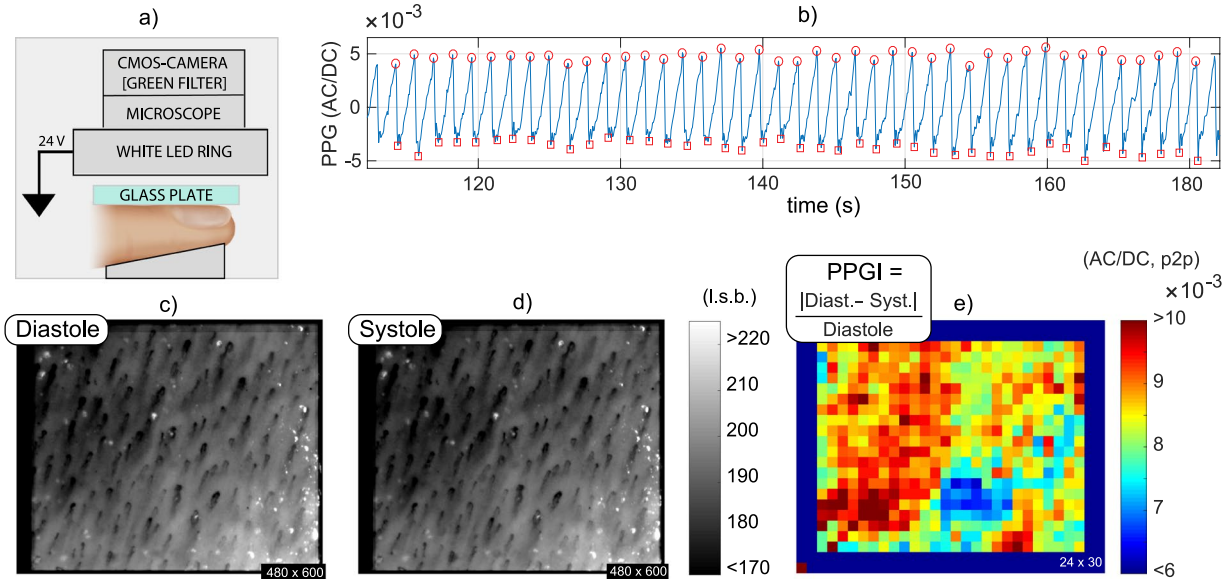


**Figure 4.** Videocapillaroscopic examination of the nger nail fold using green wavelengths: (**a**) Setup schematics; (**b**)Average PPG signal, with indication for systolic maxima (circles) and minima (squares); and super-resolved images of the upper dermis at the (**c**) peak instants and (**d**) valleys, respectively (imaging area, about $1.6 \times 2$ mm; ampli cation, $\times 60$). e downsized and normalized di erential image between (**c**,**d**) is a PPG-image (**e**) which suggests no relation between capillary density and PPG-signal strength. e gure was created by A. Moço.

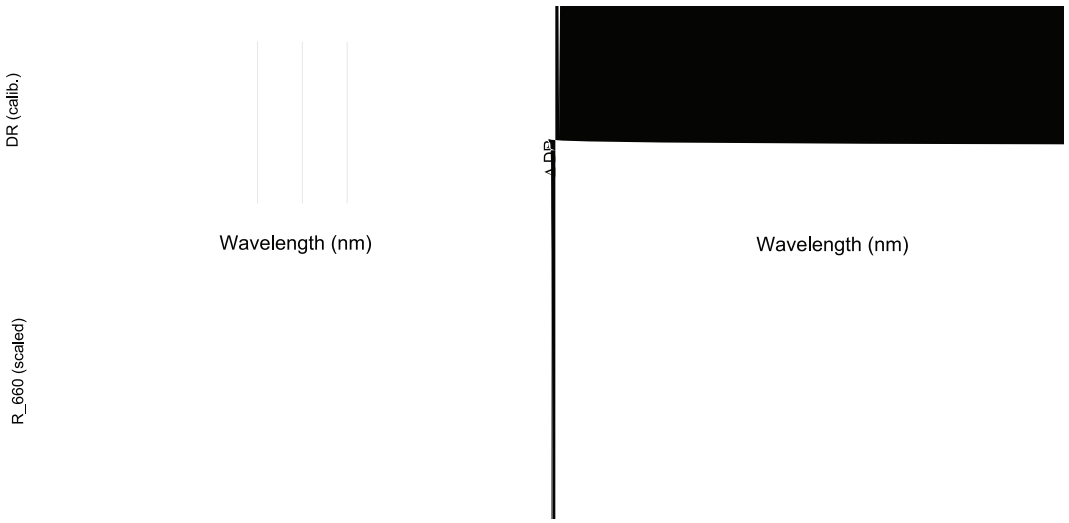


Figure 5c shows the medians of the PPG spectra obtained with the photometer-OFP system at normal and compressed skin ($N = 15$). Also included are the corresponding remote spectra estimated by using a transfer function (TF), which accounts for the skin properties and probe speci cations (see the methods section for details). To ease comparisons, the PPG-amplitude spectra are scaled by its relative minimum at 660 nm and two variables were de ned: the amplitude ratio of green over red (GoR, with green and red ranges de ned at 520–577 nm and 660–700 nm, respectively), and the ratio of IR (range, 800–840 nm) over red (IRoR). In our dataset, paired-sample t-tests indicated that compression signi cantly reduces the average GoR by a factor of 4 (means $\pm$ standard deviations; reference, $927 \pm 319$; compression, $2.32 \pm 1.24$; 1 rejected outlier; $p < 0.001$), whereas IRoR is not signi - cantly a ected (reference, $1.90 \pm 0.16$; compression, $1.95 \pm 0.14$; $p = 0.43$). is supports the multilayered BVVs hypothesis by evidencing that selectively blocking dermal layers a ects the shallow PPG-green wavelengths. Note that the invariance of IRoR to compression holds for remote acquisition because the probe geometry is irrelevant

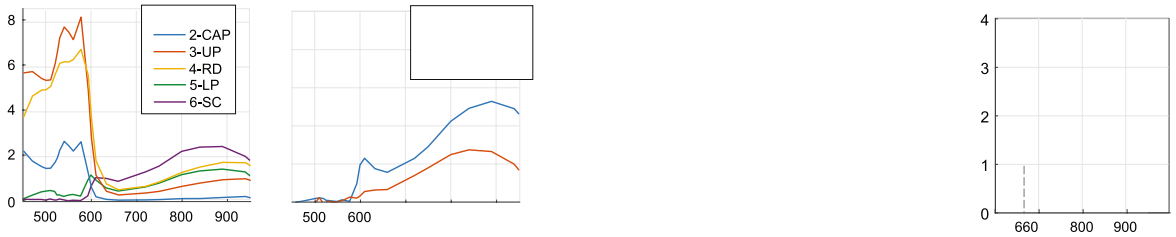


in the red-IR diagnostic window. at green and red-IR wavelengths probe di erent mixture-weights of the layers signatures explains the selective mitigation of the PPG-amplitude below 580 nm by compression.

Figure 5d contrasts the relative PPG-phase shi spectra in the 475–975 nm wavelength range. e dual-state behaviour of the relative PPG-phase function, with stable phases within the blue-green (475–580 nm) and red-IR (625–975 nm), means that the shapes of the PPG signals are fairly similar within the ranges. e phase gap at ~600 nm indicates the abrupt penetration depth change, which is in uenced slightly by the compression-induced blanching of the skin.

**Experimental Part 2: Monte Carlo simulations.** e simulated layer's signatures for normal and compressed skin are depicted in Fig. 6(a,b). e simulated remote PPG spectra resemble measurements for, e.g., pulsation patterns of $w_{ref} = (0, 0, 1, 2, 3, 1)/3$ and $w_{comp} = (0, 0, 0, 2, 18, 1)/3$, for layers (1-EPI, …, 6-SC), for reference and compression, respectively.

e simulations for the penetration depth (PD) and depth-origin (DO) of the PPG signals are insightful to assess if arteriolar BVVs can, at least theoretically, modulate PPG. Figure 7a exempli es the light ux, $F(z)$, and di erential ux between diastole and systole, $\Delta F(z)$, for 577 nm. e PD is de ned as the depth for which area under $F(z)$ is ~63.2%. Analogously, the DO is de ned as the depth for which the area under $\Delta F(z)$ is ~63.2%.

In agreement with earlier work[15,23], we veri ed that the PD of blue-green wavelengths is at the level of the capillary loops (see Fig. 7b). However, only a small fraction of the di usely re ected photons need to be modulated for PPG signal generation. e DO for the reference skin model is greater than the PD. is means that PPG in VIS e ectively reaches the pulsating arterioles of the upper plexus and the RD. ese insights also hold in IR; i.e., the center of gravity of the DO of the PPG signals in VIS-IR is deeper than the PD of the incident light. Similar insights hold for the compressed skin model (see Fig. 7c).

## Discussion

is investigation aims to assess if the opto-physiology of remote PPG in VIS-IR can be explained by arteriolar/arterial BVVs located at dermal and subdermal skin layers. Using the nger pad as inspection site, we showed

that the remote PPG-amplitude spectrum for normal and for compressed skin can be acquired and modeled in light of the volumetric model. Skin compression reduces the blood content of the skin (particularly venous blood) and enables that green wavelengths penetrate deeper and reach more pulsating vessels. Since the depth-origin of the PPG signals is within the arteriolar level in VIS and IR, an alternative model for the genesis of PPG in VIS is, therefore, unnecessary. Yet, we remark that our insights are not direct experimental evidence and do not invalidate the possibility of complementary mechanisms of PPG formation occuring in parallel.

e volumetric model holds for all skin sites but the PPG spectra is have skin-site variations. Our preliminary results suggest lower overall PPG-amplitudes and an imbalance between amplitudes in green versus red-IR wavelengths, for glabrous and non-glabrous skin (see Section 2 in the Supplementary le). Possible explanations include density of arterio-venous shunt density, microvascular bed thickness and epidermal scattering and absorption.

To the best of our knowledge, only Reuss[22] stated explicitly that the capillary loops are microcirculatory, but there is no experimental support for this assumption. At most, capillary ow velocities can be estimated and shown to have a constant and a pulsatile component. Based on nailfold videocapillaroscopy, the typical RBC average velocity measured in healthy subjects is around $0.8 \pm 0.2$ mm/s[27]. More recently, Baran *et al.*[28] applied Doppler optical microangiography (DOMAG) method to map RBC absolute velocity in the arterial and side of the nger cuticle capillaries loops and obtained about 0.67 mm/s for arteriole-end capillaries. Unfortunately, the sampling rate was limited to 0.5 frames per minute, which did not allow the assessment of pulsating ow inside the capillary loops. Still, the fact that RBC speed even reduces in capillary loops[28] with increasing ow resistance at low velocities[29] suggests the steadiness of blood ow at upper arterioles. e assumption of constant ow velocity at the capillaries is not subscribed by Huelsbusch[23], who modeled PPG assuming that the PPG is formed at the capillary loops only. Interestingly, Huelsbusch's simulated spectrum largely overestimates the magnitude of signals in blue-green wavelengths, suggesting the incorrectness of this parameter setting. We veri ed that the problem does not occur in simulations where the sources of pulsatility/BVVs are at the dermal plexuses, RD and SC.

Recently, Volkov *et al.*[30] showed that the capillary ow speed of RBCs of the ngernail fold have a pronounced pulsatile ow component overlapped with an asynchronous component. e magnitude of the capillary ow speeds (range, 1–5 mm/s) is dissonant from reference healthy ranges, but the observed morphological resemblance between capillary ow speed waveforms and pulsatile blood pressure waveforms is invariant to possible scaling inaccuracies. Still, these waveforms were erroneously interpreted as evidence for the inadequacy of volumetric theory. In fact, if the data of Volkov *et al.* is valid, then any remnants of pulsatile pressure that reach the capillary level are accommodated as pulsatile ow and not as capillary BVVs. is possibility is strengthened by morphological resemblance between Volkov's ow speed waveforms and the pulsatile pressure waveforms of Mahler *et al.*[31], who performed direct cannulation of human nger nailfold capillaries.

**Limitations and future work.** *Modeling simpli cations.* We begin by acknowledging the simplifying assumption of a reference skin model and PPG spectrum. is exercise should only hold for illustrative purposes because PPG is highly in uenced by individual and contextual factors like posture[32] and skin site (see Section 2 in the Supplementary le for details). Additional skin models with slight changes in the layers properties, e.g., thickness, relative pulsatile strength and absorption, would add to this study by translating inter-individual and skin-site variations. Still, building and running these come at the cost of added computational e ort and time while a single skin model su ces to verify that the normal and compressed PPG-amplitude spectra are obtained for realistic parameter settings.

We further remark that modeling the skin as a structure with a discrete number of stacked horizontal layers is a valid simpli cation[33], though not without the possible risk that the microanatomic description of the skin into 2 plexuses may not be representative of all skin sites[34,35]. Wong and Geyer visualized the nger pad using optical coherence tomography (OCT) and documented a tree-like rami cation where relatively thick dermal arteries arise from the subcutaneous arterial plexus and ramify until they form the ascending segment of the capillary loops. As reported, capillary loops of the nger pad could be split in "arterial units" and the upper plexus would be absent. However, the volumetric model for PPG signal formation also holds if the skin microvasculature has a tree-like arrangement, although the mixing weights of the layer contributions to the resulting PPG spectrum may di er at the upper dermis. Future work is valuable to ascertain these considerations.

*Parameter errors.* Selecting optical parameters from the literature is an error-prone task. Glaring examples are the absorption and scattering parameters, which are mostly determined in *ex vivo* tissue samples and may di er by an order of magnitude[36,37]. Moreover, the scattering coe cients of living skin can be much lower than those of *ex vivo* samples[38,39].

Although the major ndings are not a ected, the uncertainty in parameter settings in uences the DRS and PPG spectra. e computation of the skin layer's signatures is robust to small variations in blood concentration at the upper dermis. However, the same does not hold if the skin layers scattering or absorption coe cients vary by an order of magnitude. Figure 8 exempli es the considerable impact on spectral simulations of an hypothetical variation in epidermal scattering by an order of magnitude (reference $\mu_{s,EPI} = 156.34\,\mathrm{cm}^{-1}$ versus reduced $\mu_{s,EPI} = 10.42\,\mathrm{cm}^{-1}$; common parameters for the epidermal layer: $n = 1.33$; $\mu_{a,EPI} = 15.039$; $g = 0.9$; $d_{EPI} = 0.8$ mm).

e errors incurred in parameter settings do not preclude the remote PPG spectrum from being obtained. However, the errors propagate to the mixing weights of the BVVs. Consequently, the inverse estimation of the mixing weights of the BVVs is currently an ill-posed problem. Future progresses in this direction could enable the possible usefulness of the skin's pulsating pro le for functional tissue characterization.

*Probe e ects.* DR measurements were contact-based and may contain probe pressure artifacts[40,41]. Concerns are rested by verifying that the DR plot for the non-compressed skin is similar to those of Bjorgan *et al.*[42]. Probe

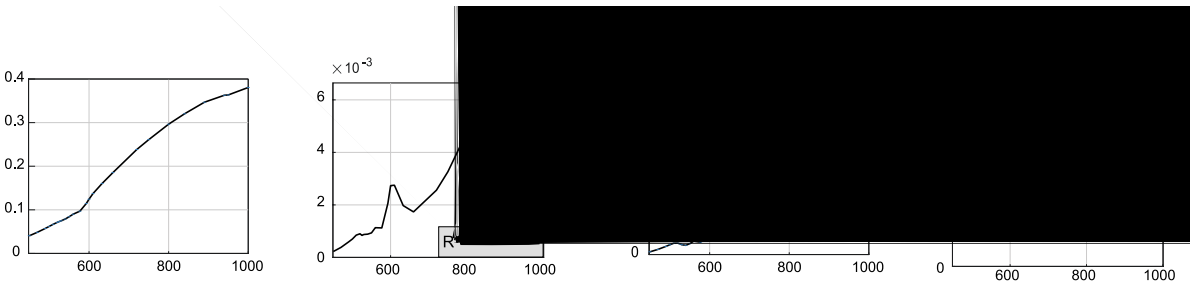


e ects reduce the PPG-amplitude ratios in green over red-IR by a factor of up to 0.7 (corresponding to about 1 mm of nger compression; see Supplementary section 1 for details on the PPG-amplitude response to incremental nger pad compression in green and IR). Modeling the geometry of the OFP (implicit in TF computations) is another possible source of error which makes it inviting to perform of spectral measurements remotely as demonstrated by Corral *et al.*[43] and Blackford *et al.*[44]. However, measuring the PPG spectra in re ectance-mode was preferable to remote multispectral measurements since the latter are noisier. Concerns to the validity of the remote spectra PPG include ballistocardiographic artifacts[17] and specular re ections.

## Conclusion

e exploration of the VIS range in PPG-based applications is relatively recent and the underlying opto-physiology remains doubtful. Our results present a step forward in this regard by supporting the volumetric model. By taking a joint numerical and experimental approach, we linked the skin's pulsating pro le and signatures at di erent skin-depths with the remote PPG-amplitude spectrum. Our results support that arteriole-arterial BVVs are feasible as origin of PPG signals in visible light and IR. e depth-origin of PPG using green wavelengths are dermal BVVs while red-IR wavelengths even interact with subcutanous BVVs. e videocapillaroscopic mapping of the PPG-amplitude at the nger nail fold further suggests that the PPG signal is not associated with capillary density.

## Methods

**Participants.** Sixteen subjects (ages, 27–55 years old; 2 females) participated in this investigation. e study was approved by the Internal Committee Biomedical Experiments of Philips Research and an informed consent was obtained from each subject. All experiments were carried out in accordance with the ethical standards laid down in the 1964 Declaration of Helsinki.

**Data acquisition.** We explored three modalities for acquiring skin re ectance data. Camera-based remote PPG measurements were made in green versus IR bands. Because of its relevance for prospective PPG-imaging applications, the derived insights are the foundation of this study. Videocapillaroscopy o ers a joint morphological and functional assessment of the upper dermis and of the associated remote PPG signal strength. DRS extends insights to the 500–940 Hz spectra, and strengthens our study by making the skin compression intervention possible.

is section details the data acquisition settings used in this investigation. We highlight that, in all data acquisition modalities, the sampling rates in the range 16–30 Hz are well above the Nyquist frequency (about 1 Hz) and enable estimating the average pulse-rate frequency using Fourier analysis in each temporal window of 10–20 sec.

e average diastole and systole instants are determined with a precision error of 63 ms, which is appropriate for noise mitigation and imaging PPG.

*Camera-based remote PPG measurements.* Skin video recordings were performed using a monochrome camera (IDS Inc, Germany; model $\mu$Eye, UI122xSE-M; 12 bit resolution; model, USB 2000+; sampling rate, 20 or 30 Hz).

e susceptibility of remote PPG to motion artifacts was addressed in nger pad recordings by supporting the forearm on a table. Additional care was taken to eliminate specular re ections by including polarizing lm in front of the light source and camera in a cross-polarization arrangement. For each video recording, skin regions of interest (sRoIs) were manually demarcated at video recordings of the nger pad and used to extract PPG signals. For each frame, the raw PPG signal is computed by averaging the time-varying intensity of the sRoI in successive frames. Each camera channel retrieves a single time series per sRoI.

*Videocapillaroscopy.* Recordings were performed at the nger nail fold of one subject from our dataset. Our system comprised a CMOS camera (coupled with a green lter; sampling rate, 20 Hz), a microscope lens (magni cation factor, 40x) and a white high power LED ring light (CCS HPR2-100SW; uorescent white; voltage, 24 VDC; see Fig. 4a). Motion artifacts were addressed by supporting the forearm on a table. Minute cardiac-related bulk motion cannot be fully suppressed, but the di use lighting at the imaged nger nailfold prevents artifacts in remote PPG signals and amplitude maps. Specular re ections were minimized by applying a thin layer of

ultrasound gel at the nail fold and a microscope slide, which promote the translucency of the epidermis (refractive index = 1.3) and by using a LED-ring close to the nger site (distance of about 1 cm). e orientation of the LEDs (70–80 degrees w.r.t. the camera, which is frontal to the nailfold) helped to minimize specular re ections. e observation that PPG originates from non-capillary regions within videocapillaroscopic data and the derived PPG-amplitude images was con rmed in di erent measurement sessions and ngers.

*DRS.* Contact-based re ectance data was probed with a spectrometer (Ocean Optics, Inc.; model, USB 2000+; 12 bit resolution; so ware, SpectraSuite, 2008) coupled with an OFP. For each recording, we obtained parallel sets of $N = 2048$ time series at collocated, narrow and non-overlapping frequency bands, including the 475–975 nm range. e OFP (diameter, 400 $\mu$m) was shielded by a cylindrical ferrule which blocked ray paths back-scatted up to 1.59 mm from its center.

e nger pressures applied with our DRS-OFP equipment at normal/reference measurement conditions at the nger pad are low and estimated to be below 10 kPa ( nger compression depth, below 1 mm). In contrast, the applied pressure intensity used for eliciting the compression regime in the DRS reference-compression intervention is estimated to be within about 40 to 60 kPa (compression depth, about 2 mm). ese compression estimates were based on a devoted experiment of PPG-amplitude and DR measurements under gradually increasing nger pad compression (see Supplemental Section 1).

**Processing skin reflectance data.** Our experimental data is raw skin re ectance (sampled well above the pulse-rate frequency) from which we aim to ensemble PPG signals. e nuances in signal processing requirements for camera-based PPG acquisition and DRS are described below.

*Camera-based video recordings.* Raw PPG signals in video recordings were extracted by averaging pixels in used-de ned sRoIs and AC/DC-normalized (i.e., divided by its slowly-varying component, obtained with low-pass- ltering with a Butterwordth lter with cutto frequency at ~40 bpm). e amplitude of the re ection-mode PPG signals is typically low (particularly in red wavelengths), but its signal-to-noise ratio (SNR) can be improved by adaptive bandpass ltering (ABPF). ABPF consists of ltering out the frequency components of the signals that are not multiples of the fundamental of the pulse-rate frequency.

ABPF was applied in an overlap-and-add manner (stride length, 256 samples; overlap factor, 50%) with Hanning windowing. We selected the fundamental and 6 harmonics of the pulse-rate frequency and a tolerance band of one bin around each center frequency. When available, the reference signals used for identifying the systolic peaks and instantaneous pulse-rate were nger pulse oximetry signals (acquired synchronously with video recordings). Alternatively, the reference were the PPG-signals probed at green wavelengths, as these have the best available SNR. A er ABPF, the PPG cycles in streams were condensed into ensemble-averaged (EA) waveforms, separately for each camera channel and signal dimension. EA relies on Gaussian noise cancelation in the averaging process and in the signals periodicity. In practice, cycles were demarcated based on the timing of the systolic peaks (identi ed in reference signals), temporally registered, and, nally, averaged by using the trimmed mean operator (outlier rejection, 10%). Each super-resolved EA waveform condenses, at least, 100 consecutive cycles.

*Processing of DRS recordings.* As a preprocessing step, DRS streams require calibration for additive sensor noise. is is done by subtracting the noise oor in each wavelength, $\lambda$. By denoting the raw re ectance as $DR_0(t, \lambda)$, its calibration is expressed as

$$DR(t, \lambda) = \frac{DR_0(t, \lambda) - DR_{DARK}(\lambda)}{DR_{REF}(t, \lambda) - DR_{DARK}(\lambda)}, \quad (1)$$

where $DR_{DARK}(\lambda)$ denotes the noise level in full darkness. Similarly, $DR_{REF}(\lambda)$ denotes the re ectance measurement of a reference standard (model WS-1, re ectivity >98% from 250–1500 nm, Ocean Optics, Inc.) placed frontally to the OFP at a distance of 2 mm. DR recordings were processed to obtain re ectance PPG-amplitude and PPG-phase spectra.

**Monte Carlo simulations of skin reflectance and remote PPG.** e spectrum and depth-origin of remote PPG was simulated by the Monte Carlo method. ese e orts were preceded by Huelsbusch[23], but his assumption that the remote PPG signal comes exclusively from the capillary loops, as well as his overestimated blood concentration and scattering coe cients of the skin, resulted in the underestimation of PPG signals in red-IR. We overcame these issues using parameters from the DRS literature and/or estimated based on our experiments. We simulated the photon migration through the tissue for the diastolic and systolic states at a set of tissue characteristics, including $SpO_2$ and blood concentration in the tissue, where the systolic state was obtained by an incremental increase of arterial blood over the diastolic state. Data were computed over multiple skin layers and in the 450–1000 nm range.

We used the publicly available GPU-MCML code package, which enables simulating photon propagation in a multi-layered turbid media with adjustable spatial dimensions and resolution[45]. e geometry of the scenario is speci ed in cylindrical coordinates with the emitter centered at the origin and normal to the tissue surface[33]. e emitter con guration approximates collimated light from an in nitely narrow beam. e input (.mci) les for MCML incorporated skin architecture parameters, absorbance and scattering coe cients, and physiological parameters such as $SpO_2$, blood concentration, melanin content, etc. Separate models were implemented for reference and compressed skin.

| Skin layers | $n$ | $d_l$ (cm) | $C_b$ | $C_w$ | $v_d$ ($\mu$m) |
|---|---|---|---|---|---|
| 1-EPI | 1.33 | 0.08 | 0 | 0.20 | 0 |
| 2-CL | 1.37 | 0.015 | 0.004 | 0.65 | 10 |
| 3-UP | 1.40 | 0.008 | 0.02 | 0.65 | 20 |
| 4-RD | 1.40 | 0.12 | 0.004 | 0.65 | 20 |
| 5-DP | 1.40 | 0.05 | 0.04 | 0.65 | 40 |
| 6-SC | 1.44 | 0.5 | 0.03 | 0.05 | 50 |

**Table 1.** Layer settings for normal/reference skin.

| Skin layers | $n$ | $d_l$ (cm) | $C_b$ | $C_w$ | $v_d$ ($\mu$m) |
|---|---|---|---|---|---|
| 1-EPI | 1.33 | 0.08 | 0 | 0.05 | 0 |
| 2-CL | 1.37 | 0.008 | 0.0012 | 0.15 | 10 |
| 3-UP | 1.40 | 0.004 | 0.0024 | 0.15 | 20 |
| 4- RD & DP | 1.40 | 0.1 | 0.024 | 0.15 | 20 |
| 5-SC | 1.44 | 0.2 | 0.036 | 0.35 | 40 |

**Table 2.** Layer settings for compressed skin.

*Tissue Model.* Figure 2 illustrates a multilayered model of normal glabrous (non hairy) skin tissue. e model consists of six homogeneous layers with di erent fractions of water, $C_w$, blood, *Cb*, and fat, *Cf*. Table 1 lists layer thicknesses, water and blood fractions for each skin layer–numbered from 1 to 6 (deepest)–in the diastolic state.

e rst layer listed is the epidermis. At the palm or nger pad, its thickness is high in comparison with other skin sites[46]. e palm also features a vefold lower density of melanocytes than at other skin areas[47]. Accordingly, melanin was not included in our model. For the remaining layers, the optical and anatomical properties of our skin geometry are similar to previous work[21,23,48], though the average blood concentration in the dermis, $C_b$, is lower. is setting conforms with recent DRS studies[42,49] indicating that $C_b$ is within 1–3%.

e refractive index for all internal surface interfaces increases gradually from 1.33 at the surface to 1.44 at the bottom interface. e arterio-venous ratio ($r_a$:$r_v$) corresponds to the diastolic state and was applied to all dermal layers in the diastolic state[50]. For the reference condition, $r_a$:$r_v$ was set at 50%:50%. Additional settings are as follows: the arterial oxygen saturation $SpO_2$ was set at 97% and the venous oxygen saturation, $SvO_2$, was set 30% lower; and the fat concentration, $C_f$, was set at 40% at the subcutis[42]. e vessel diameters per dermal layer, $v_d$, were estimated from the literature[51].

Table 2 lists the adaptations made to mimic the skin compression status. In short, the dermal water and blood volume concentrations reduced, whereas pooling of blood (mostly venous) was implemented at the subcutis. e $r_a$:$r_v$ ratio was set at 100%:0 at the dermal layers and 75%:25% at the SC.

*Absorption settings.* e absorption coe cients of the skin layers were set di erently for the epidermis and for the dermal layers. e epidermal absorption coe cient, $\mu_{a,EPI}$, was estimated as a combination of background tissue, $\mu_{a,base,EPI}$, and water:

$$\mu_{a,EPI}(\lambda) = C_w \mu_{a,water}(\lambda) + (1 - C_w)\, \mu_{a,base,EPI}(\lambda). \tag{2}$$

$\mu_{a,water}$ was determined from Palmer[52] and Smith[53]. e baseline tissue absorption for the epidermis, $\mu_{a,base,EPI}$, translates the e ect of connective tissue and was implemented from Jacques[37]:

$$\mu_{a,base,EPI}(\lambda) = \gamma\left[0.244 + 85.3\, \exp\left(-\frac{\lambda - 154}{66.2}\right)\right]. \tag{3}$$

e wavelength, $\lambda$, is speci ed in nm and the factor $\gamma = 0.5$ accounts for water losses during *ex vivo* measurements. e absorption coe cient for the dermal layers and subcutis during diastole, $\mu_a^{(d)}(l, \lambda)$, $l2 \ldots 6$, were estimated as a sum of non-blood tissue absorption coe cient, $\mu_a^{(d)}(l, \lambda)$, and blood absorption, weighted by their respective concentrations within the layer. For convenience, the subscripts ($l$) and ($\lambda$) are omitted in the remainder of this section. $\mu_{a,nb}^{(d)}$, is set as follows:

$$\mu_{a,nb}^{(d)} = C_f\ \mu_{a,fat} + (1 - C_f)\, C_w\ \mu_{a,water} + (1 - C_f)\ (1 - C_w)\mu_{a,base}. \tag{4}$$

For the dermal background absorption, $\mu_{a,base}$, the exponential dependency of Eq. 3 was taken from Salomatina *et al.*[54]:

$$\mu_{a,base} = \gamma \frac{C_w}{C_{w0}}\left[0.244 + 16.82\ \exp\left(-\frac{\lambda - 400}{80.5}\right)\right] \tag{5}$$

where $\gamma$ was set as 0.5 for dermal layers ($l = 2 \ldots 5$) and 0.25 for the subcutis ($l = 6$). e coe cient $C_{w0} = 0.65$ accounts for the fact that background measurements of $\mu_{a,base}(l)$ are performed at about 65%. ese settings are aimed at meeting the absorption coe cient measurements of the bloodless dermis and subcutis of Simpson *et al.*[55].

We account for the fact that a fraction of the incident light is re ected in the vessel walls, meaning that the *apparent* blood volume that interacts with light is lower than the actual blood concentration at the skin. is e ect is called self-shielding and is in con ict with the assumption of homogeneous mixture between bloodless skin tissue and blood[56]. A correcting factor for this e ect is easily performed by setting a function, $f[.]$, that translates e ective dermal blood concentration ($Cb$) *apparent* ($Cb'$). $f[.]$ is in uenced by the product of the average vessel diameter and by the blood absorption of the layers, $\mu_a v_d$. For collimated light, $f[.]$ is an exponentially decaying function given by

$$f[\mu_a v_d] = \frac{1}{1 + 1.007(\mu_a v_d/2)^{1.228}}. \tag{6}$$

Self-shielding is negligible in the red-IR range since $\mu_a$ is very low; i.e., $f[\mu_a v_d] \approx 1$. For wavelengths at the 500–580 nm range, $f[\mu_a v_d]$ reaches about 0.7 at the LD and SC (where the vessel diameter is ~40 $\mu$m) but only about 0.85 at the upper dermis, which is where most blue-green photons interact with tissue. us, the discrete absorbers correction has a minor in uence on the accuracy of PPG simulations, although we implemented it for the sake of completeness. Accordingly, the diastolic arterial and venous blood fractions, $f_a^{(d)}$ and $f_v^{(d)}$, and the $Cb'^{(d)}$ at pulsating layers were set as follows:

$$f_a^{(d)} = r_a \; Cb \; f\left[v_d \; \left((1 - SpO_2)\mu_{a,Hb} + SpO_2\mu_{a,HbO_2}\right)\right], \tag{7}$$

$$f_v^{(d)} = r_v \; Cb \; f\left[v_d \; \left((1 - SvO_2)\mu_{a,Hb} + SvO_2\mu_{a,HbO_2}\right)\right], \tag{8}$$

$$Cb'^{(d)} = f_a^{(d)} + f_v^{(d)}. \tag{9}$$

Using the absorbance spectra of deoxygenated and oxygenated hemoglobin, $\mu_{a,Hb}$ and $\mu_{a,HbO_2}$, respectively, compiled by Bosschaart *et al.*[57], the diastolic absorption coe cient of the total tissue was given by

$$\begin{aligned} \mu_a^{(d)} = {} & f_a^{(d)} \; \left((1 - SpO_2) \; \mu_{a,Hb} + SpO_2\mu_{a,HbO_2}\right) + \ldots \\ & f_v^{(d)} \; \left((1 - SvO_2) \; \mu_{a,Hb} + SvO_2\mu_{a,HbO_2}\right) + Cb' \; \mu_{a,water} + (1 - Cb) \; \mu_{a,nb}^{(d)}. \end{aligned} \tag{10}$$

Systole is modeled as fractional pulsatile increases, $p$, of arterial blood in pulsating layers. e systolic $f_a^{(s)}$ and $Cb'^{(s)}$ are

$$f_a^{(s)} = f_a^{(d)} + p \; f\left[v_d \; \left((1 - SpO_2)\mu_{a,Hb} + SpO_2\mu_{a,HbO_2}\right)\right], \tag{11}$$

$$Cb'^{(s)} = Cb' + p \; f\left[v_d \; \left((1 - SpO_2)\mu_{a,Hb} + SpO_2\mu_{a,HbO_2}\right)\right]. \tag{12}$$

Two possible mechanisms ensure model consistency during the systolic increase of arterial blood volume. Either pulsatile changes are compensated by water displacements[50,58] (WD) or there is layer expansion (LE) to accommodate the additional uid; i.e., micro-modulations of layers thickness[59]. In LE, the layers thickness during systole is set in proportion to $p$:

$$d^{(s)} = d \; (1 + Cb'^{(s)} \; p). \tag{13}$$

By de ning the expansion factor for each layer, $E$, as $d/d^{(s)}$, the absorption coe cient during systole is

$$\begin{aligned} \mu_a^{(s)} = {} & E \; [f_a^{(s)} \; \left((1 - SpO_2)\mu_{a,Hb} + SpO_2 \; \mu_{a,H_bO_2}\right) + \ldots \\ & f_v^{(s)} \; \left((1 - SvO_2)\mu_{a,Hb} + SvO_2 \; \mu_{a,H_bO_2}\right) + Cb'^{(s)} \; \mu_{a,w} + (1 - Cb'^{(s)}) \; \mu_{a,nb}^{(d)}]. \end{aligned} \tag{14}$$

In practice, the simulations obtained under WS or LE are similar (see Fig. 9). is is unsurprising since the blood concentration at the dermis is only about 2–3% and $E$ is close to unity. Accordingly, only LE was implemented.

*Scattering settings.* Skin scattering is conceptually regarded as a summation of Rayleigh and Mie scattering[60]. In spite of fundamental di erences, the di use light setting is well approximated by assuming that scattering losses occur in the depth dimension only, thus justifying that dermal scattering is reasonably described by a one-term expression, or even set as wavelength-independent[21]. We derived the reduced scattering coe cient for the dermal tissue, $\mu'_s$, from the observations of Simpson and Shimada[39,55]:

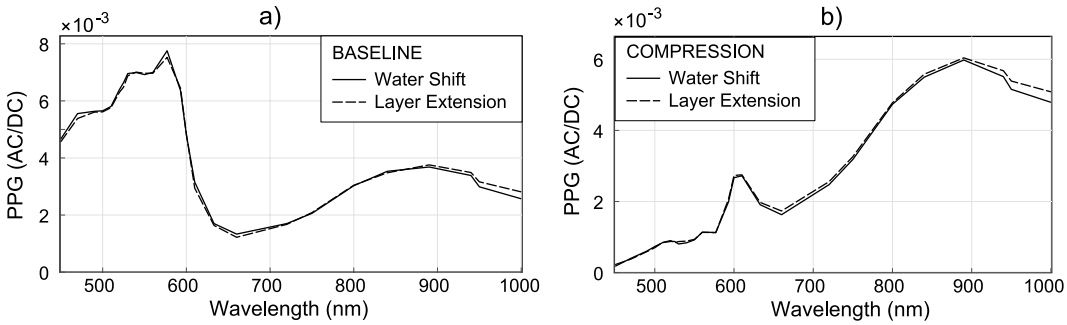


**Figure 9.** e similarity of simulation outcomes with WS and LE on (**a**) normal and (**b**) compressed skin models.

$$\mu_s' = c_0(l, \lambda)\ \lambda^{-b}, \tag{15}$$

where $c_0(l,\lambda)$ is a calibration constant that sets the reduced scattering $\mu'_s$ to (EPI: 15 cm$^{-1}$; CL, UD, RD, LD: 20 cm$^{-1}$; SC: 10 cm$^{-1}$)[55]. e decaying factor $b$ was estimated as 0.1 below 580 nm and 0.05 otherwise. Similar to Simpson *et al.*[55], the anisotropy factor was assumed to be 0.9 for tissue.

*Simulating remote PPG.* For each simulated wavelength, $\lambda \in <450,1000>$ nm, and skin layer, $l = 1 \ldots 6$, the relevant outputs from MCML for expressing the simulated remote PPG spectra are the fraction of photons reaching the surface per cm as a function of radial distance from the origin, $Rdr(r, \lambda, l)$, and the total di use re ectance, $Rdt(\lambda, l)$, expressed as fraction of total emitted photons.

Matlab was used for further processing. e diastolic-systolic di use re ectance outputs were applied to mimic the PPG spectra for remote and for contact-based acquisition. e remote normalized pulsatile re ectance PPG, $PPG_{REM}$, was AC/DC normalized for pulsating layer, $l$, as normalized fractions of the total incident photons; i.e.,

$$PPG_{REM}(\lambda, l) = \frac{RdT^d(\lambda, l) - RdT^s(\lambda, l)}{RdT^d(\lambda, l)}. \tag{16}$$

where $RdT^s$, and $RdT^d$ denote the total di use re ectance during systole and diastole, respectively. Since each wavelength needs to be simulated under diastolic and systolic conditions, for a skin model with ve pulsating layers at least six simulation runs were required, per wavelength. Each simulation run consisted of 10E8 to 40E8 photons and required approximately 10 min of processing time on a Linux server operating an NVIDIA GeForce GTX TITAN with compute capability 3.5 (14 SMs).

*Optical penetration depth and depth-origin of PPG.* e Matlab routines *lookmcml.m* and *getmcml.m* (publicly available at http://omlc.org/so ware/mc/) were used to compute the optical uxes as a function of the skin depth from the MCML simulation output les. Care was taken to remove spurious peaks in the skin layer boundaries, thus ensuring that the ux functions are continuous along the depth axis.

For each wavelength and skin con guration, a ux function was computed for the diastolic state, $F^{(d)}(z)$, allowing us to express the optical penetration depth of the incident light as the skin depth, oriented along the z-axis, that is reached by $1 - \frac{1}{e}$ of the incident photons. Mathematically, the PD was obtained by solving the following equation:

$$\frac{\sum_{z=0}^{PD} F^{(d)}(PD)}{\sum_{z=0}^{T_s} F^{(d)}(z)} = 1 - \frac{1}{e} \approx 63.2\%, \tag{17}$$

where $T_s$ is the total tissue thickness. e depth-origin (DO) of the PPG signals was computed based on the ux perturbations induced during systole for each pulsatile skin layer. By weighting these according to the relative proportions of pulsatile strength in the various modeled layers, $w_l$, the di erential ow due to BVVs is given by

$$\Delta F(z) = \sum_l (F^{(d)}(z) - F_l^{(s)}(z))\ w_l^T, \tag{18}$$

where $F_l^{(s)}$ denotes the ux perturbed during systole in layer $l$. Lastly, the DO of the PPG signal was determined as the depth for which the cumulative sum of $\Delta F$ is $1 - \frac{1}{e}$; i.e.,

$$\frac{\sum_{z=0}^{DO} \Delta F(DO)}{\sum_{z=0}^{T_s} \Delta F(z)} = 1 - \frac{1}{e}. \tag{19}$$

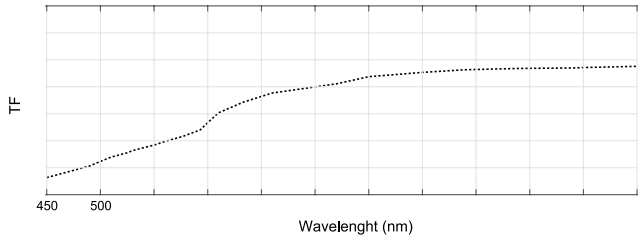


**Indirect measurements of the remote PPG spectra by using transfer functions.** Since the used OFP is shielded by a ferrule (which clips shallow photon paths) a correction is needed if the re ection-PPG spectra, $PPG_{OFP}$, are to be used for drawing considerations to the remote setting. In this investigation, the [pseudo] remote PPG-amplitude spectrum, $PPG_{REM}$, is estimated from $PPG_{OFP}$ based on a transfer function such that $TF = PPG\_REM/PPG_{OFP}$. e numerical estimation of such TF began with simulating, in MCML, the remote di use re ectance (DR) in the 450−1000 nm. e uncalibrated remote DR from the skin, during systole and diastole, were obtained as functions of the source distance. ose were integrated from $Rd_r(n_r, \lambda)$ as

$$uDR^d(i, \lambda) = \sum_{n_r=i}^{R=3000} Rd_r^d(n_r, \lambda), \tag{20}$$

$$uDR^s(i, \lambda) = \sum_{n_r=i}^{R=3000} Rd_r^s(n_r, \lambda), \tag{21}$$

where the index $n_r$ refers to source distance. For a radial resolution of 0.0005 cm and 3000 grid points, the spanned radius ranges up to 1.5 cm. e correction factors for diastolic and systolic DR, $C^d(\lambda)$ and $C^s(\lambda)$, are obtained as

$$C^d(\lambda) = RdT^d(\lambda)/uDR^d(n_\varepsilon, \lambda), \tag{22}$$

$$C^s(\lambda) = RdT^s(\lambda)/uDR^s(n_\varepsilon, \lambda). \tag{23}$$

with $n_\varepsilon$ set to 10 to prevent numerical inaccuracies. e calibrated DR for systole and diastole becomes

$$DR_{OFP}^{(s)}(\lambda) = C^{(s)}(\lambda)\ uDR^{(s)}(n_{r0}, \lambda), \tag{24}$$

$$DR_{OFP}^{(d)}(\lambda) = C^{(d)}(\lambda)\ uDR^{(d)}(n_{r0}, \lambda). \tag{25}$$

with $n_{r0} = 278$. Finally, the re ectance PPG signal the OFP and layer $l$ was obtained as

$$PPG_{OFP}(l, \lambda) = \frac{DR_{OFP}^{(d)}(\lambda) - DR_{OFP}^{(s)}(\lambda)}{DR_{OFP}^{(d)}(\lambda)}. \tag{26}$$

e TF from re ectance to [pseudo] remote-PPG was nally given by

$$TF(n_{r0}, \lambda) = \frac{\sum_l PPG_{REM}(l, \lambda) w_l}{\sum_l PPG_{OFP}(l, n_{r0}, \lambda) w_l}. \tag{27}$$

e compression curves for normal and compressed skin are shown in Fig. 10. Both indicate that the OFP con guration boosts the PPG-amplitude, particularly in blue-green wavelengths.

*Simulation precision.* e average simulation errors for the remote PPG spectra–expressed as standard deviations over the means–is 4.7% for the 475–1000 nm range. is error estimate was based on four repeated runs of the compressed skin model.

## References

1. Allen, J. Photoplethysmography and its application in clinical physiological measurements. *Physiol. Meas.* **28**, 1–40 (2007).
2. Verkruysse, W., Svaasand, L. O. & Nelson, J. S. Remote plethysmographic imaging using ambient light. *Opt. Express* **16**, 21434–21445 (2008).
3. Wukitsch, M. W., Petterson, M. T., Tobler, D. R. & Pologe, J. A. Pulse oximetry: analysis of theory, technology, and practice. *J Clin Monit* **4**, 290–301 (1988).
4. Rouast, P. V., Adam, M. T., Chuiong, R., Cornforth, D. & Lux, E. Remote heart rate measurement using low-cost RGB face video: a technical literature review. *Front. Comput. Sci.* 1–17 (2016).

5. Verkruysse, W. *et al*. Calibration of contactless pulse oximetry. *Anesth. Analg* **124**, 136–145 (2016).
6. Amelard, R. *et al*. Feasibility of long-distance heart rate monitoring using transmittance photoplethysmographic imaging (ppgi). *Scienti c Reports* **5**, 14637 (2015).
7. de Haan, G. & Jeanne, V. Robust pulse-rate from chrominance-based rPPG. *IEEE Transactions on Biomedical Engineering* **60**, 2878–2886 (2014).
8. van Gastel, M., Stuijk, S. & de Haan, G. New principle for measuring arterial blood oxygenation, enabling motion-robust remote monitoring. *Sci. Rep.* **6**, 38609 (2016).
9. Allen, J. & Howell, K. Microvascular imaging: techniques and opportunities for clinical physiol. meas. *Physiol. Meas.* **35**, 91–141 (2014).
10. atcher, J. E. *et al*. Multispectral and photoplethysmography optical imaging techniques identify important tissue characteristics in an animal model of tangential burn excision. *Journal of Burn Care & Research* **37**, 38–52 (2016).
11. Damianou, D. *e wavelength dependence of the photoplethysmogram and its implication to pulse oximetry*. Phd thesis, University of Nottingham. Department of Electrical and Electronic Engineering (1995).
12. Naslund, J., Pettersson, J., Lundeberg, T., Linnarsson, D. & Lindberg, L. G. Non-invasive continuous estimation of blood ow changes in human patellar bone. *Med Biol Eng Comput* **44**, 501–509 (2006).
13. Lindberg, L.-G., Sveider, P. & Oberg, P. A. Optical properties of blood in motion. In *OE/LASE 92*, vol. **32**, 116–122 (SPIE) (1993).
14. Shvartsman, L. D. & Fine, I. Optical transmission of blood: e ect of erythrocyte aggregation. *IEEE Trans Biomed Eng* **50**, 1026–1033 (2003).
15. Kamshilin, A. A. *et al*. A new look at the essence of the imaging photoplethysmography. *Sci. Rep.* **5**, 10494 (2015).
16. Kamshilin, A. A., Miridonov, S., Teplov, V., Saarenheimo, R. & Nippolainen, E. Photoplethysmographic imaging of high spatial resolution. *Biomed. Opt. Express* **2**, 996–1006 (2011).
17. Moco, A., Stuijk, S. & de Haan, G. Ballistocardiographic artifacts in PPG imaging. *IEEE Trans Biomed Eng* **63**, 1804–1811 (2016).
18. Moço, A., Stuijk, S. & de Haan, G. Motion robust PPG-imaging through color channel mapping. *Biomed. Opt. Express* **7**, 1737–1754 (2016).
19. Anderson, R. R. & Parrish, J. A. e optics of human skin. *J Invest Dermatol* **77**, 13–19 (1981).
20. Agache, P. *Skin Structural Components: Physiology and Metrology*, 17–399 (Springer-Verlag, Berlin, 2014).
21. Meglinski, I. V. & Matcher, S. J. Computer simulation of the skin re ectance spectra. *Computer Methods and Programs in Biomedicine* **70**, 179–186 (2003).
22. Reuss, J. L. Multilayer modeling of re ectance pulse oximetry. *IEEE Trans. Biom. Eng.* **52**, 153–159 (2005).
23. Huelsbusch, M. An image-based functional method for opto-electronic detection of skin-perfusion. Phd thesis, RWTH Aachen dept. of EE. (in German) (2008).
24. Bergstrand, S., Lindberg, L. G., Ek, A. C., Linden, M. & Lindgren, M. Blood flow measurements at different depths using photoplethysmography and laser Doppler techniques. *Skin. Res. Technol.* **15**, 139–147 (2009).
25. Raamat, R., Jagomägi, K. & Talts, J. Calibrated photoplethysmographic estimation of digital pulse volume and arterial compliance. *Clinical Physiology and Functional Imaging* **27**, 354–362 (2007).
26. Baran, U., Choi, W. J. & Wang, R. K. Potential use of oct-based microangiography in clinical dermatology. *Skin Research and Technology* **22**, 238–246 (2016).
27. Mugii, N. *et al*. Association between nail-fold capillary findings and disease activity in dermatomyositis. *Rheumatology* **50**, 1091–1098 (2011).
28. Baran, U., Shi, L. & Wang, R. K. Capillary blood ow imaging within human nger cuticle using optical microangiography. *J. biophotonics* **8**, 46–51 (2015).
29. Secomb, T. W., Hsu, R. & Pries, A. R. Motion of red blood cells in a capillary with an endothelial surface layer: e ect of ow velocity. *Am J Physiol Heart Circ Physiol* **281**, 629–636 (2001).
30. Volkov, M. V. *et al*. Video capillaroscopy clari es mechanism of the photoplethysmographic waveform appearance. *Scienti c Reports* **7**, 13298 (2017).
31. Mahler, F., Muheim, M. H., Intaglietta, M., Bollinger, A. & Anliker, M. Blood pressure uctuations in human nailfold capillaries. *American Journal of Physiology-Heart and Circulatory Physiology* **236**, 888–893 (1979).
32. Hickey, M., Phillips, J. P. & Kyriacou, P. A. e e ect of vascular changes on the photoplethysmographic signal at di erent hand elevations. *Physiol. Meas.* **36**, 425–440 (2015).
33. Jacques, S. L. & Wang, L. *Monte Carlo Modeling of Light Transport in Tissues*, 73–100 (Springer US, Boston, MA, 1995).
34. Wong, R., Geyer, S., Weninger, W., Guimberteau, J.-C. & Wong, J. K. e dynamic anatomy and patterning of skin. *Experimental Dermatology* 92–98 (2015).
35. Geyer, S. H., Nöhammer, M. M., Tinhofer, I. E. & Weninger, W. J. e dermal arteries of the human thumb pad. *Journal of Anatomy* **223**, 603–609 (2013).
36. Bashkatov, A. N., Genina, E. A. & Tuchin, V. V. Optical properties of skin, subcutaneous, and muscle tissues: A review. *Journal of Innovative Optical Health Sciences* **04**, 9–38 (2011).
37. Jacques, S. L. Optical properties of biological tissues: a review. *Phys Med Biol* **58**, 37–61 (2013).
38. Zonios, G. & Dimou, A. Light scattering spectroscopy of human skin *in vivo*. *Optics Express* **17**, 1256–1267 (2009).
39. Shimada, M., Yamada, Y., Itoh, M. & Yatagai, T. Melanin and blood concentration in a human skin model studied by multiple regression analysis: assessment by monte carlo simulation. *Phys Med Biol* **46**, 2397–406 (2001).
40. Delgado Atencio, J. A. *et al*. In uence of probe pressure on human skin di use re ectance spectroscopy measurements. *Optical Memory and Neural Networks* **18**, 6–14 (2009).
41. Reif, R. *et al*. Analysis of changes in re ectance measurements on biological tissues subjected to di erent probe pressures. *Journal of Biomedical Optics* **13**, 010502–010502–3 (2008).
42. Bjorgan, A., Milanic, M. & Randeberg, L. L. Estimation of skin optical parameters for real-time hyperspectral imaging applications. *Journal of Biomedical Optics* **19**, 066003–066003 (2014).
43. Corral, L. F., Paez, G. & Strojnik, M. Optimal wavelength selection for non-contact re ection photoplethysmography. In *Proc. SPIE*, vol. 8011, 801191–801191–7 (2011).
44. Blackford, E. B., Estepp, J. R. & McDu , D. J. Remote spectral measurements of the blood volume pulse with applications for imaging photoplethysmography. In *SPIE BiOS*, vol. 10501, 8 (SPIE) (2018).
45. Alerstam, E. *et al*. Next-generation acceleration and code optimization for light transport in turbid media using gpus. *Biomedical Optics Express* **1**, 658–675 (2010).
46. Verma, G. *Fundamentals of Histology* (New Age International (P) Limited, Publishers, 2001).
47. Yamaguchi, Y. & Hearing, V. J. Melanocytes and their diseases. *Cold Spring Harb Perspect Med* **4**, a017046 (2014).
48. Tuchin, V. V. *et al*. Finger tissue model and blood perfused skin tissue phantom. In *Proc. SPIE*, vol. 7898, 78980–78980–11 (2011).
49. Yudovsky, D. & Pilon, L. Retrieving skin properties from *in vivo* spectral re ectance measurements. *J Biophotonics* **4**, 305–314 (2011).
50. Schmitt, J. M., Zhou, G. X., Walker, E. C. & Wall, R. T. Multilayer model of photon di usion in skin. *J. Opt. Soc. Am. A.* **7**, 2141–2153 (1990).
51. Braverman, I. M. *Anatomy and physiology of cutaneous microcirculation*, book section 1, 3–22 (CRC Press, Boca Raton, Florida, 1995).

52. Palmer, K. F. & Williams, D. Optical properties of water in the near infrared. *Journal of the Optical Society of America* **64**, 1107–1110 (1974).
53. Smith, R. C. & Baker, K. S. Optical properties of the clearest natural waters (200-800 nm). *Appl Opt* **20**, 177–184 (1981).
54. Salomatina, E., Jiang, B., Novak, J. & Yaroslavsky, A. N. Optical properties of normal and cancerous human skin in the visible and near-infrared spectral range. *J Biomed Opt* **11**, 064026 (2006).
55. Simpson, C. R., Kohl, M., Essenpreis, M. & Cope, M. Near-infrared optical properties of *ex vivo* human skin and subcutaneous tissues measured using the Monte Carlo inversion technique. *Phys Med Biol* **43**, 2465–2478 (1998).
56. Wim, V. *et al*. Modelling light distributions of homogeneous versus discrete absorbers in light irradiated turbid media. *Physics in Medicine and Biology* **42**, 51–65 (1997).
57. Bosschaart, N., Edelman, G. J., Aalders, M. C. G., van Leeuwen, T. G. & Faber, D. J. A literature review and novel theoretical approach on the optical properties of whole blood. *Lasers in Medical Science* **29**, 453–479 (2014).
58. Reuss, J. L. & Siker, D. e pulse in re ectance pulse oximetry: Modeling and experimental studies. *Journal of Clinical Monitoring and Computing* **18**, 289–299 (2004).
59. Graa , R., Dassel, A. C. M., Zijlstra, W. G., Mul, F. F. M. & Aarnoudse, J. G. *How Tissue Optics In uences Re ectance Pulse Oximetry*, 117–132 (Springer US, Boston, MA, 1996).
60. Wang, L. V. & Wu, H. I. *Rayleigh eory and Mie eory for a Single Scatterer*, 17–35 (John Wiley & Sons, Inc., 2009).

## Acknowledgements

We are thankful to Stefanos Andreou and Dr Erwin Bente (COBRA Research Institute, Eindhoven University of Technology) for allowing access to a videomicroscope. Our gratitude is extended to Dr Marius Boamfa (Multiphysics and Optics Group, Philips Corporate Technologies) for kindly borrowing light equipment, as well as to Martijn Koedam and Mark van Gastel for their e orts into GPU con guration (Electronic Systems Group, Eindhoven University of Technology). Lastly, we thank Dr Wim Verkruisse (Standartization Research, Philips Research, Eindhoven) for constructive discussions.

## Author Contributions

A.M. conceived and conducted experiments, analyzed the results and dra ed the manuscript. G.d.H. conceived the idea of PPG signals as a mixture of skin layers signatures and contributed to the interpretation of experimental results. All authors contributed to experimental planning and reviewed the manuscript.

## Additional Information

**Supplementary information** accompanies this paper at https://doi.org/10.1038/s41598-018-26068-2.

**Competing Interests:** e authors declare no competing interests.

**Publisher's note:** Springer Nature remains neutral with regard to jurisdictional claims in published maps and institutional a liations.